International Journal of Solids and Structures 47 (2010) 2223–2233

Contents lists available at ScienceDirect

International Journal of Solids and Structures

journal homepage: www.elsevier.com/locate/ijsolstr

Forming simulation of aluminum sheets using an anisotropic yield function coupled with crystal plasticity theory

Kaan Inal [a,*], Raja K. Mishra [b], Oana Cazacu [c]

[a] University of Waterloo, Waterloo, Ontario N2L 3G1, Canada
[b] General Motor R&D Center, Warren, MI 48090, USA
[c] University of Florida, REEF, Shalimar, FL 32579-1163, USA

ARTICLE INFO

Article history:
Received 9 August 2009
Received in revised form 28 February 2010
Available online 21 April 2010

Keywords:
Anisotropic yield function
Crystal plasticity
Textured aluminum sheet
R-values
Electron backscatter data
Micro–macro scale modeling

ABSTRACT

This paper describes the application of a coupled crystal plasticity based microstructural model with an anisotropic yield criterion to compute a 3D yield surface of a textured aluminum sheet (continuous cast AA5754 aluminum sheet). Both the in-plane and out-of-plane deformation characteristics of the sheet material have been generated from the measured initial texture and the uniaxial tensile curve along the rolling direction of the sheet by employing a rate-dependent crystal plasticity model. It is shown that the stress–strain curves and *R*-value distribution in all orientations of the sheet surface can be modeled accurately by crystal plasticity if a "finite element per grain" unit cell model is used that accounts for non-uniform deformation as well as grain interactions. In particular, the polycrystal calculation using the Bassani and Wu (1991) single crystal hardening law and experimental electron backscatter data as input has been shown to be accurate enough to substitute experimental data by crystal plasticity data for calibration of macroscopic yield functions. The macroscopic anisotropic yield criterion CPB06ex2 (Plunkett et al., 2008) has been calibrated using the results of the polycrystal calculations and the experimental data from mechanical tests. The coupled model is validated by comparing its predictions with the anisotropy in the experimental yield stress ratio and strain ratios at 15% tensile deformation. The biaxial section of the 3D yield surface calculated directly by crystal plasticity model and that predicted by the phenomenological model calibrated with experimental and crystal plasticity data are also compared. The good agreement shows the strength of the approach. Although in this paper, the Plunkett et al. (2008) yield function is used, the proposed methodology is general and can be applied to any yield function. The results presented here represent a robust demonstration of implementing microscale crystal plasticity simulation with measured texture data and hardening laws in macroscale yield criterion simulations in an accurate manner.

1. Introduction

A successful strategy for increased usage of light weight materials in automotive components involves accurate numerical modeling of their forming behavior under complex strain paths encountered in the manufacturing environment. The forming simulation models are necessarily macroscopic scale models that use experimental input data from mechanical tests to describe the anisotropy effects arising from the initial texture and its evolution. Use of embedded multiscale mathematical models to simulate material properties at engineering length scale solely from atomic and electronic structure inputs is still a distant dream. Yet, the advances in theory, experiment, and computation in recent years have created the possibility to bridge the microscale–macroscale gap through a hierarchical multiscale approach and provide input data, which is not available experimentally at engineering length scale or it is hard to generate. Accuracy of the formulations at multiple length scales is key to the success of such approaches.

The mechanical properties of a polycrystalline metal depend on many attributes of its microstructure and considerable efforts have been made in the study of its micro-mechanics to aid macroscale modeling. These microscale studies indicate that, among the factors which result in plastic deformation in single and polycrystals, crystallographic slip and factors that promote the slip processes are most important to accurately simulate macroscopic scale deformation. The crystal structure and chemical composition of alloys affect critical resolved shear stresses (CRSS) to activate slip and slip induced lattice rotations. Different grains in polycrystalline materials evolve their orientations differently, resulting in a non-random distribution of the crystal orientations even from an

* Corresponding author. Tel.: +1 519 888 4567x38114; fax: +1 519 885 5862.
E-mail addresses: kinal@mechengl.uwaterloo.ca (K. Inal), raj.k.mishra@gm.com (R.K. Mishra), cazacu@reef.ufl.edu (O. Cazacu).

0020-7683/$ - see front matter © 2010 Elsevier Ltd. All rights reserved.
doi:10.1016/j.ijsolstr.2010.04.017

initial random (isotropic) polycrystal. Such texture development has profound effects on the mechanical, thermal, and other physical properties of metals. On the other hand, many metal forming processes such as drawing, extrusion, rolling, and sheet metal forming induce texture development. Plastic anisotropy due to texture dominates deformation behavior up to moderately large strains. Macroscale modeling that is informed by microscale (crystal plasticity modeling) modeling is indispensable to account for this induced plastic anisotropy. Furthermore, microscopic and mesoscopic scale studies have the added advantage of guiding material (microstructure) design for optimum performance but such discussion is beyond the scope of this paper.

To describe the plastic anisotropy of rolled metal sheets at macroscopic level, Hill (1948) has developed a quadratic yield criterion, which is an extension to orthotropy of the isotropic von Mises distortional energy theory. The validity of this yield function has been explored by numerous experiments, the consensus being that it is well suited to specific metals and textures, especially steel. Formulations that were intended to improve the description of anisotropic yielding of materials with a FCC crystal structure, in particular aluminum and its alloys, have been proposed (see for example Barlat et al. (1997, 2003, 2005, 2007), Cazacu and Barlat (2001, 2004)). Finite element (FE) analyses of deep drawing of cylindrical cups using the yield functions proposed by Barlat et al. (2003, 2005) (see Yoon et al. (2004, 2006)) or Cazacu and Barlat (2001, 2004) (e.g. Soare et al. (2007)) or Soare et al. (2008) have shown that improved accuracy can be obtained by using a yield function that captures both the anisotropy in yield stresses and *R*-values. However, only Barlat et al. (2005) and Soare et al. (2008) 3D yield criteria have the capability to predict more than four ears (i.e. six or eight ears). A yield criterion for describing the anisotropic plastic response of textured metals for full three-dimensional stress states was recently proposed by Plunkett et al. (2008). This anisotropic criterion is applicable to hexagonal closed packed materials (HCP) that exhibit strength differential effects (e.g. Mg and its alloys) as well as to materials for which there is no noticeable difference between the behavior in tension and compression when subjected to monotonic loading. This orthotropic yield criterion is an extension of the isotropic yield function of Cazacu et al. (2006), which is obtained by using two linear transformations on the Cauchy stress. The resulting orthotropic criterion involves 18 anisotropy parameters, a degree of homogeneity (or exponent "a") that can be varied, and a strength differential parameter. To determine the coefficients involved in this criterion, Plunkett et al. (2008) have used results from multiple mechanical tests that probe the anisotropy of the given material.

However, for anisotropic materials, virtual data obtained by means of crystal plasticity calculations can provide data points covering the entire stress space. The full-constraint Taylor model in conjunction with finite element method (e.g. Inal et al. (2000, 2002)) have been used for such purposes. Grytten et al. (2008) used the classical Taylor model to evaluate and calibrate Barlat et al.'s (2005) yield function and applied it to model plastic anisotropy of aluminum alloys. Plunkett et al. (2006, 2007) have used the self-consistent viscoplastic texture model of Lebensohn and Tomé (1993) to calibrate the Cazacu et al. (2006) yield function and model the evolution of the anisotropy coefficients associated with twinning induced texture changes in zirconium. Guan et al. (2008) successfully implemented the notion of using a crystal plasticity model to fit the parameters of Barlat's Yld96 anisotropic yield function and used it for hydroforming simulations.

Very recently, Rousselier et al. (2009) proposed a new self-consistent polycrystal model. In this model, improved computational efficiency has been obtained by drastically reducing the number of crystallographic orientations and applying a specific parameter calibration procedure to obtain a good agreement with all stress–strain and transverse strains curves. However, there is an issue as to whether or not the predictions of such models are accurate enough to replace mechanical tests Taylor-type polycrystalline models employ a homogeneous local deformation gradient in each grain, which is identical to the macroscopic deformation gradient. This assumption, besides violating equilibrium between the grains, excludes the effects of grain interactions and morphologies (see Wu et al. (2001)). Limitations of Taylor-type models to predict *R*-values for aluminum alloys have also been demonstrated by Inal et al. (2000) and Grytten et al. (2008), etc. Even with the more advanced self-consistent models (e.g. Molinari et al. (1987) and Lebensohn and Tomé (1993)) generally, it is difficult to obtain simultaneously a good description of flow stresses and *R*-value anisotropy (see for example Lopes et al. (2003) and Darrieulat and Montheillet (2003)).

In this paper, the polycrystal plasticity model formulated by Asaro and Needleman (1985) is employed in the FE analyses. Electron backscatter diffraction (EBSD) data, initial texture data, and the tensile stress–strain curve in the rolling direction 0° (L) sample are used to calibrate this crystal plasticity model. Two sets of FE simulations of the polycrystalline aggregates are carried out to calculate the macroscopic yield surfaces from microstructure data as well as data from a single tensile test. In the first set of simulations, the experimentally observed grain morphologies are exactly implemented into the FE analysis by incorporating EBSD maps in the FE mesh. Thus, several elements of the finite element mesh are considered to represent a single crystal within the polycrystal aggregate and the constitutive response at a material point is given by the single crystal constitutive law. This approach enforces equilibrium and compatibility between grains throughout the polycrystalline aggregate in the weak finite element sense. (see for e.g. Neale et al. (2003) and Inal et al. (2008)). In this way, we can account for non-uniform deformation as well as grain interactions. In the second set of simulations, the Taylor assumption of uniform deformation in each grain is adopted. The crystal plasticity models and the two methodologies to perform virtual FE experiments and thus obtain yield stress points are presented in Sections 3 and 4 and the most suitable hardening law for accurate prediction of the mechanical anisotropy using this approach is identified. The anisotropic yield criterion by Plunkett et al. (2008) as well the calibration procedures based on either crystal plasticity data or mechanical test results are summarized in Section 5. An illustration of this methodology to describe the anisotropy of a commercial grade continuous cast (CC) AA5754 aluminum sheet is presented in Section 6. Comparisons between the predictions of the macroscale yield function calibrated with mechanical data and virtual data demonstrate that the predictions of a robust crystal plasticity model are accurate enough to replace mechanical tests as input for macroscale models.

2. Experimental measurement of texture and mechanical anisotropy

The material used in this study was chosen to be a 1 mm thick continuous cast AA5754 sheet in the fully recrystallized condition. The chemical composition of the sheet is shown in Table 1. The sheet has an average grain size of 22 micrometers and a grain aspect ratio of 1.7. The electron backscatter diffraction (EBSD) data from the top flat surface of the sheet was collected from

Table 1
Chemical composition of the 5754 alloy sheet (balance Al).

Mg wt. (%)	Mn wt. (%)	Cr wt. (%)	Fe wt. (%)	Si wt. (%)
3.1	0.25	<0.01	0.24	<0.10

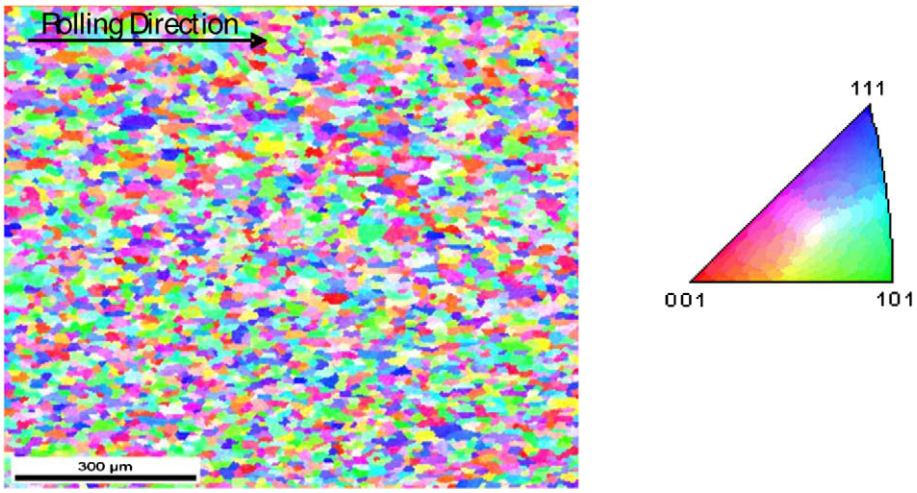

Fig. 1. Inverse pole figure map from the flat surface of the as-received sheet showing fully recrystallized grains. The colors of the grains correspond to the lattice orientation of the grains as shown in the color key on the right. (For interpretation of the references to colour in this figure legend, the reader is referred to the web version of this article.)

electropolished samples using a LEO 1450VP scanning electron microscope operating at 20 kV and fitted with a TSL EBSD detector. The texture analysis was done using the TSL OIM Analysis v4.6 software. The Inverse pole figure (IPF) map of the sample is shown in Fig. 1 and the corresponding texture plots are shown in Fig. 2. Note that, for these sheets, the through thickness texture gradient was negligible. Standard tensile specimens as per ASTM Standard E8 specification were machined from the sheets. The specimens had an overall length of 203.2 mm, a gage length of 50.8 mm and a gage width of 12.7 mm. The tensile properties were evaluated at 0° (rolling direction, L), 15°, 30°, 45°, 60°, 75° and 90° (T) to the rolling direction with an MTS 810 System at SECAT Inc., Lexington, KY.

The 0.2% offset yield strength, the ultimate tensile strength, total elongation, *n*-value, and *R*-value (at 15% strain) were determined for each specimen and are listed in Table 2. As will be explained in Section 3 below, the EBSD data, texture data, and the tensile stress–strain curve for the 0° (RD) sample are used to calibrate the crystal plasticity model. The experimentally measured mechanical anisotropy data is used to validate the predictions of the coupled model.

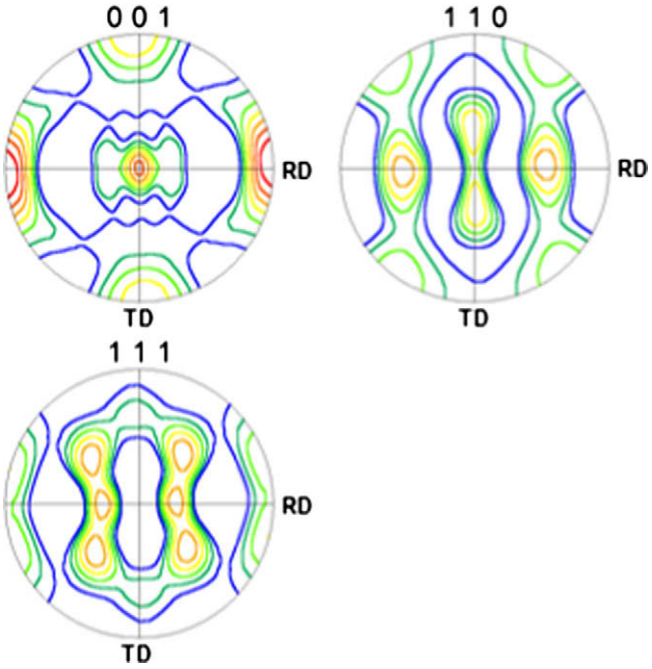

Fig. 2. Texture plot calculated from the EBSD data shown in Fig. 1 using TSL software for orthtropic symmetry.

Table 2
Tensile properties of the samples machined at different orientations from the rolling direction.

Sample orientation (rolling direction = 0°)	YS (0.02%) MPa	UTS MPa	Elongation (%)	*n*-value (uniform range)	*R*-value (15% strain)
0°	98.6	208.9	19.0	0.30	0.81
15°	97.4	206.8	20.3	0.30	0.64
30°	96.3	204.8	21.9	0.30	0.54
45°	95.1	202.2	23.1	0.29	0.58
60°	94.7	201.8	23.9	0.29	0.67
75°	96.3	202.7	23.0	0.29	0.78
90°	97.9	205.2	22.6	0.29	1.08

3. Crystal plasticity model

The polycrystal plasticity model formulated by Asaro and Needleman (1985) is employed in this analysis. The total deformation of a crystallite is taken to be the result of two distinct physical mechanisms: crystallographic slip due to dislocation motion on the active slip systems, and elastic lattice distortion. Within an FCC crystal, plastic deformation occurs by crystallographic slip on the twelve $\{111\}\langle 110\rangle$ slip systems. In the rate-sensitive crystal plasticity model employed, the elastic constitutive equation for each crystal is specified by:

$$\overset{\nabla}{\sigma} = LD - \dot{\sigma}^0 - \sigma \mathbf{tr} D, \tag{1}$$

where $\overset{\nabla}{\sigma}$ is the Jaumann rate of Cauchy stress, D represents the strain-rate tensor and L is the elastic modulus tensor. The term $\dot{\sigma}^0$ is a viscoplastic type stress-rate that is determined by the slip rates on the slip systems of the FCC crystal. A more detailed presentation of the crystal plasticity constitutive model can be found in Inal et al. (2002) and Tugcu et al. (2004). The slip rates are taken to be governed by the power-law expression

$$\dot{\gamma}_{(\alpha)} = \dot{\gamma}_{(0)} sgn\tau_{(\alpha)} \left| \frac{\tau_{(\alpha)}}{g_{(\alpha)}} \right|^{1/m}, \tag{2}$$

where $\dot{\gamma}_{(0)}$ is a reference shear rate taken to be the same for all the slip systems, $\tau_{(\alpha)}$ is the resolved shear stress on slip system α, $g_{(\alpha)}$ is its hardness and m is the strain-rate sensitivity index. The function $g_{(\alpha)}$ characterizes the current strain-hardened state of all the slip systems. The rate of increase of the function $g_{(\alpha)}$ is defined by the hardening law:

$$\dot{g}_{(\alpha)} = \sum_{\beta} h_{(\alpha\beta)} |\dot{\gamma}_{(\beta)}|, \tag{3}$$

where $g_{(\alpha)}(0)$ is the initial hardness, taken to be a constant τ_0 for each slip system, and the $h_{(\alpha\beta)}$ values represent the hardening moduli. The form of the moduli is given by

$$h_{(\alpha\beta)} = q_{(\alpha\beta)} h_{(\beta)} \ \text{(no sum on } \beta), \tag{4}$$

where $h_{(\beta)}$ is a single slip hardening rate and $q_{(\alpha\beta)}$ is the matrix describing the latent hardening behavior of the crystallite. For the simulations presented in this paper, latent hardening was neglected ($q_{(\alpha\beta)} = 1$).

Three different single slip hardening laws are employed to simulate the stress–strain curves and calculate the R-values in this paper. The first one assumes the following power-law form for the function $h_{(\beta)}$

$$h_{(\beta)} = h_0 \left(\frac{h_0 \gamma_a}{\tau_0 n} + 1 \right)^{n-1}, \tag{5}$$

where h_0 is the system's initial hardening rate, n is the hardening exponent and γ_a is the accumulated slip.

Based on measurements of strain hardening of single crystals from aluminum alloys by Chang and Asaro (1981), the following slip hardening rate was used by Asaro and co-workers:

$$h_\beta = h_s + (h_0 - h_s) sech^2 \left\{ \left(\frac{h_0 - h_s}{\tau_s - \tau_0} \right) \gamma_a \right\}, \tag{6}$$

where h_0 and h_s are the system's initial and asymptotic hardening rates. If $h_s = 0$, then τ_s represents the saturation value of the shear stress.

A simple form for the self-hardening $h(\gamma_\alpha)$ that gives a monotonically decreasing modulus at small strains and a finite rate of hardening at large γ_a (Bassani and Wu, 1991) has the form

$$h(\gamma_\alpha) = h_s + (h_0 - h_s) sech^2 \left\{ \left(\frac{h_0 - h_s}{\tau_I - \tau_0} \right) \gamma_\alpha \right\}, \tag{7}$$

where τ_0 is the initial critical resolved shear stress, τ_I is the so-called stage I stress, h_0 is the initial hardening rate, and h_s is assumed to depend on the total accumulated slip γ_a on all slip systems:

$$h_s = h_s^I + \left(h_s^{III} - h_s^I \right) tanh \left(\frac{\gamma_a}{\gamma_0^{III}} \right), \tag{8}$$

where h_s^I and h_s^{III} are the hardening rates during the stage I and III, respectively, and γ_0^{III} is approximately the accumulated slip at the onset of stage III. Henceforth, these three hardening laws will be referred to as P (Power law hardening) model, A (Asaro hardening) model and B (Bassani–Wu hardening) model. The material parameters used for these hardening models are presented in Table 3.

4. Simulations with crystal plasticity models

As mentioned in the introduction, two sets of simulations of the polycrystalline aggregates are carried out in this work. In the first set of simulations, a "finite element (FE) per grain" model is employed for the numerical analyses. In this model, each element, or group of elements of the finite element mesh represents a single crystal, and the constitutive response at a material point is given by the single crystal constitutive law. This approach enforces equilibrium and compatibility between grains throughout the polycrystalline aggregate in the weak finite element sense. For the second set of simulations, the Taylor theory of crystal plasticity is adapted to model the behavior of the polycrystal aggregate. Henceforth, these two models will be referred to as FE per grain model and Taylor model respectively.

4.1. FE per grain formulation

In this model, the so-called unit cell approach is adopted. The unit cell is constructed to contain a sufficiently large number of grains such that sufficient information on essential microstructural and textural features characterizing the sheet is represented. It is microscopically finitely large but macroscopically infinitely small enough to represent a single material point in the sheet (Inal et al., 2008). The experimentally observed grain morphologies are exactly implemented into the finite element analyses by incorporating electron backscatter diffraction IPF maps as in Fig. 1 in the numerical simulations.

The sheet itself is subject to plane stress conditions. The loading imposed on the edges of the unit cell is assumed to be constant (Fig. 2), such that

$$\begin{aligned} \frac{\dot{\varepsilon}_{11}}{\dot{\varepsilon}_{22}} &= \rho_1, \\ \frac{\dot{\varepsilon}_{22}}{\dot{\varepsilon}_{11}} &= \rho_2, \end{aligned} \tag{9}$$

where $\dot{\varepsilon}_{11}$ and $\dot{\varepsilon}_{22}$ are the (principal) logarithmic strain-rates. The constant boundary conditions imposed at the four edges (sides) of the unit cell naturally result in periodic boundary conditions. Thus, uniaxial tension along rolling direction corresponds to $\rho_1 = -0.5$; while $\rho_1 = 0$ and $\rho_1 = 1$ describe an in-plane plane strain tension in rolling direction and balanced biaxial tension respectively. Likewise, uniaxial tension along transverse direction corresponds to $\rho_2 = -0.5$; while $\rho_2 = 0$ and $\rho_2 = 1$ describe an in-plane plane strain tension in transverse direction and balanced biaxial tension respectively. The macroscopic strains of the unit cell are obtained from $\dot{\varepsilon}_{11}$ and $\dot{\varepsilon}_{22}$, and the macroscopic stresses, σ_{ij}^M, are computed by averaging the corresponding values of stresses σ_{ij} over the total number of integration points N (over the total number of elements):

$$\sigma_{ij}^M = \frac{1}{N} \sum \sigma_{ij}, \tag{10}$$

where the grain stresses σ_{ij} are computed according to the single crystal plasticity model presented in Section 3. Note that plane stress conditions are applied by setting $\dot{\sigma}_{33}^M$ to 0.

In the numerical analyses, quadrilateral elements, each consisting of four linear velocity triangular sub-elements, are employed. These elements (with four integration points per element) are

Table 3
Material parameters used in the crystal plasticity simulations.

Model	τ_0 (MPa)	m	n	q	h_0/τ_0	τ_s/τ_0	h_s/τ_0	h_s^I/τ_0	γ_0^{III}	h_s^{III}/τ_0
P-Model	33.0	0.02	0.272	1.0	36.0	N/A	N/A	N/A	N/A	N/A
A-Model	41.6	0.02	N/A	1.0	5.75	2.275	0.795	N/A	N/A	N/A
B-Model	40.0	0.02	N/A	0.0	12.0	1.19	N/A	0.885	1.45	0.04

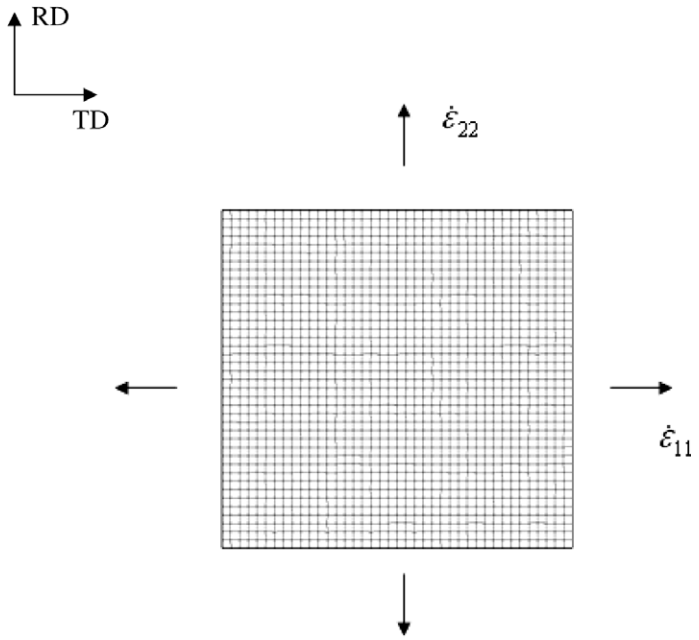

Fig. 3. Schematic representation of a unit cell.

modified to incorporate a higher order integration scheme. Making use of this integration scheme and the "crossed triangle" configuration of the elements, different material properties (i.e. Euler angles) can be mapped efficiently to a single element. Thus, fewer elements are needed to model grain-grain and/or grain-particle interactions. Furthermore, an equilibrium correction technique is employed to prevent any drift away from the true equilibrium path during the incremental procedure (Inal et al., 2002).

4.1.1. Virtual experiments using FE per grain model on CC AA 5754 sheet

The initial texture for the continuous cast aluminum alloy AA5754 is shown in Fig. 3 where RD and TD correspond to the rolling and transverse direction of the sheet respectively. The EBSD map, representing 221 grains/orientations (Fig. 4), has been incorporated to a finite element mesh using 2484 elements. Even though all the elements are the same size in the initial mesh, the 2484 elements are not equally divided between grains; the number of elements assigned to grains depend on the size of the grains. A comparison between the uniaxial stress–strain curves predicted by crystal plasticity and the uniaxial stress–strain curve measured experimentally is presented in Fig. 5. Note that the strain-rate sensitivity parameter m (presented in Table 3) employed in the simulations is in agreement with measurements on most FCC metals at low homologous temperatures (Yoshida et al., 2007). The crystal elastic constants were taken as $C_{11} = 206$ GPa, $C_{12} = 118$ GPa and $C_{44} = 54$ GPa. The predicted deformed meshes where contour plots of true strain are displayed demonstrate that the strain patterns predicted by Models P and A are very similar while the prediction by the B-Model is slightly different (Fig. 6).

Numerical simulations of true stress–strain curves show that the CC AA5754 sheets present relatively low anisotropy. The differences

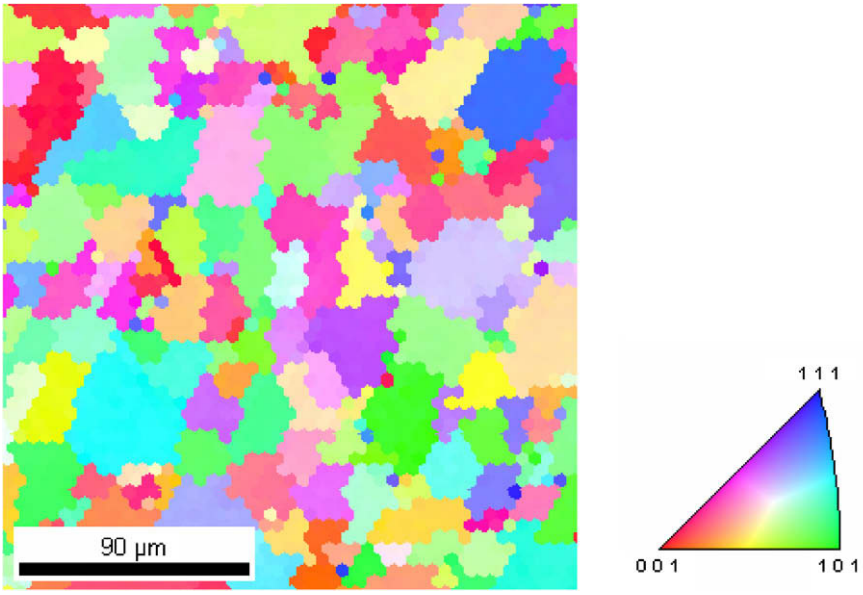

Fig. 4. Electron backscatter diffraction inverse pole figure [001] map employed in the crystal plasticity simulations.

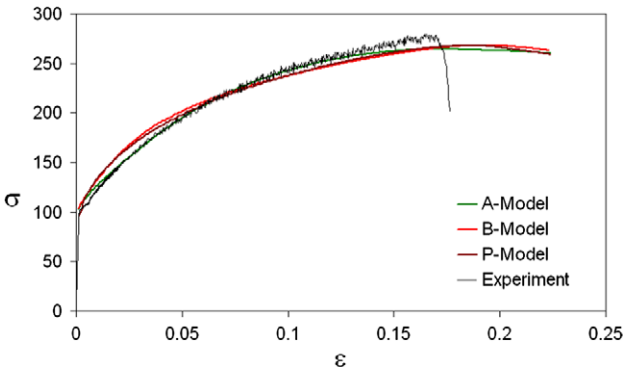

Fig. 5. Simulated and experimental true stress–strain curves in uniaxial tension for RD.

in the shapes of the stress–strain curves calculated using the three hardening laws are minor. The tensile curve for the 0° sample (parallel to RD direction) is slightly higher than those of the TD and 45° samples for simulations using all three hardening models (these results are not presented here since the differences between the curves are very small), which is consistent with experimental data.

4.1.2. R-value simulations

In replicating a set of *R*-values for several orientations, the specimens are oriented at different angles to the rolling direction (Fig. 7). Orientations of 0°, 15°, 30°, 45°, 60°, 75° and 90° with respect to the rolling direction are considered. The boundary condition defined in Eqs. 6 and 7 are replaced by

$$\frac{\dot{\sigma}_{11}}{\dot{\sigma}_{22}} = \kappa_1, \qquad \frac{\dot{\sigma}_{22}}{\dot{\sigma}_{11}} = \kappa_2, \tag{11}$$

where $\dot{\sigma}_{11}$ and $\dot{\sigma}_{22}$ are the macroscopic true stress-rates. Thus, for the *R*-value simulations of 0° and 90° orientations, $\kappa_2 = 0$ and $\kappa_1 = 0$ are employed respectively, while the *R*-value simulations of 15°, 30°, 45°, 60° and 75° orientations are performed by rotating the initial texture. The simulated *R*-values (obtained at 15% of strain along the tensile direction to be consistent with experimental *R*-values at this strain value) are presented in Fig. 8 where there are subtle differences in the variation of *R*-value with orientation for the three hardening models. Bassani–Wu (B-Model) hardening law is seen to capture the experimental variation of the *R*-value most accurately. It should be mentioned that a vast majority of *R*-value predictions using crystal plasticity models reported in the literature show disagreement with experimental observations (Inal et al., 2000). This is mainly due to that fact that these simulations were performed with the assumption of uniform deformation and did not account for grain interactions and morphology when the texture is rotated. The unit cell approach applied in our simulations can account for non-uniform deformation as well as grain interactions. The choice of hardening law is seen to be important for correctly predicting the trend even though the stress–strain curves are not sensitive to the choice of the hardening law.

4.2. Crystal plasticity simulations with the taylor model

It has already been shown that the FE per grain model can be employed to obtain in-plane (rolling direction – transverse direction of the sheets) stress–strain curves during uniaxial tension to provide the necessary parameters for the macroscale phenomenological model (presented in Section 5 below). For out-of-plane stress conditions, experimental data can rarely be obtained. In this

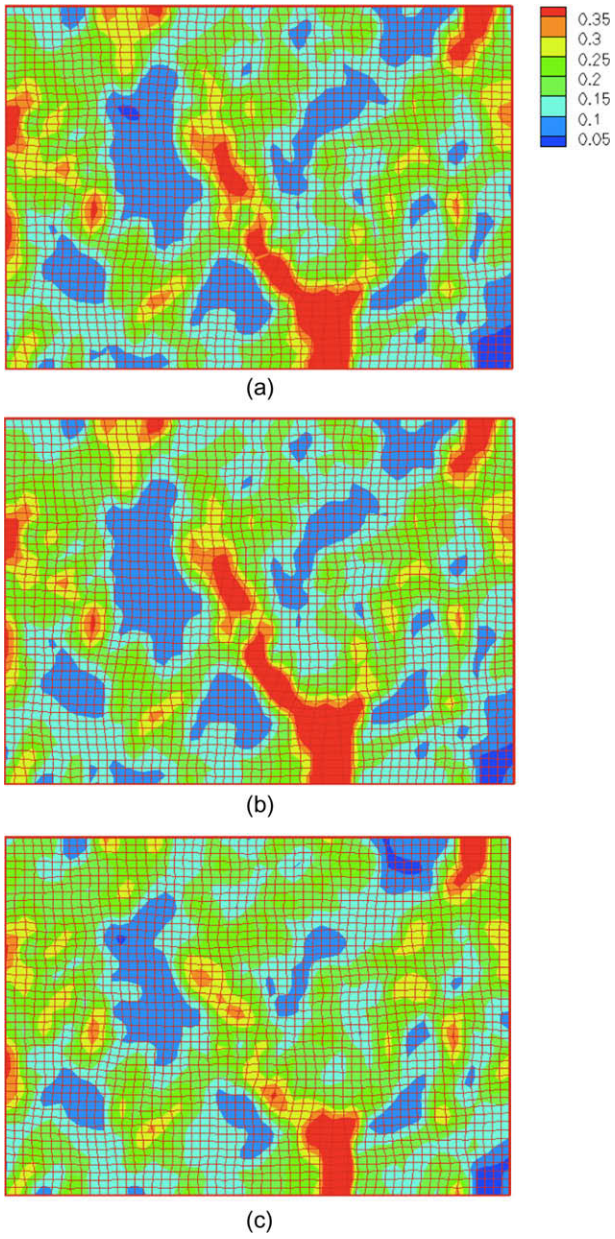

Fig. 6. Simulated deformed meshes at a true strain of 17% for (a) P-Model, (b) A-Model and (c) B-Model.

section, we demonstrate that in-plane texture measurements and the corresponding crystal plasticity parameters can be used to simulate simple shear. The simple shear simulations in this section were performed by integrating the single crystal constitutive law defined in Section 3 at a single integration point with the assumption of homogeneous deformation. The same number of discrete orientations (221 grains) as employed in the in-plane simulations have been used. Fig. 9 presents the results of simple shear simulations along the rolling direction in the rolling direction–transverse direction and rolling direction-normal direction planes. Simulations show that the proposed model can predict the anisotropy of the macroscopic stress–strain response (Fig. 9).

5. Macroscopic modeling with CPB06ex2 anisotropic yield function

The 3D orthotropic yield criterion proposed by Plunkett et al. (2008), denoted in the following as CPB06ex2, is used to describe

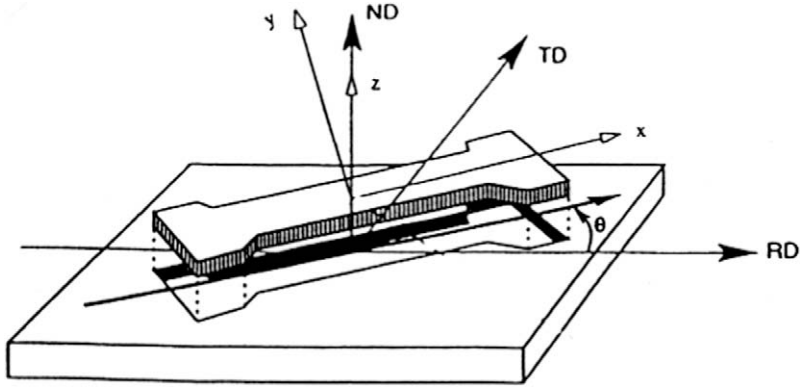

Fig. 7. Schematic diagram of an *R*-value test specimen relative to the sheet.

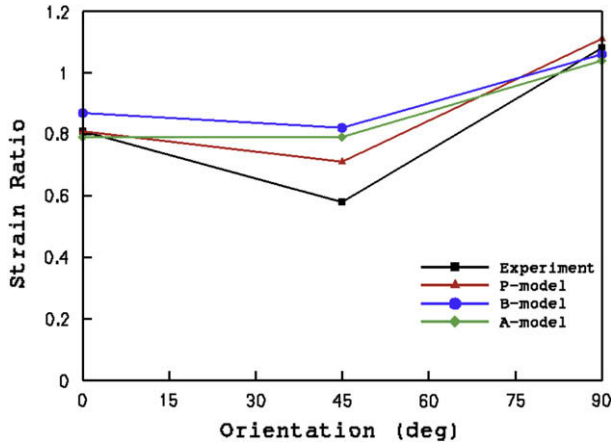

Fig. 8. Comparison of experimental and predicted *R*-values.

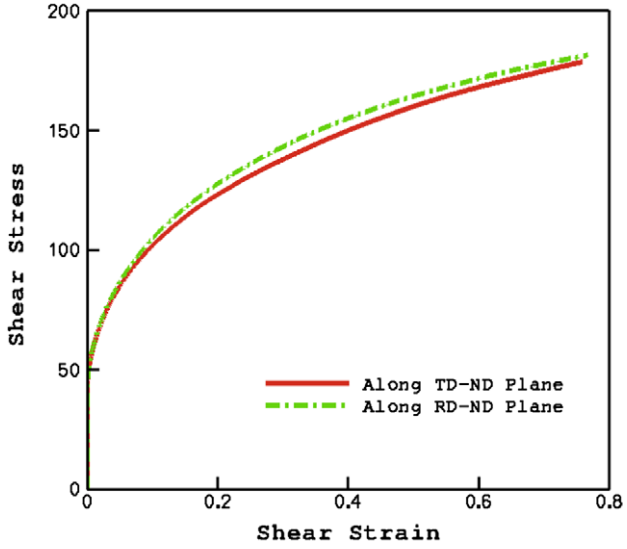

Fig. 9. Simulated simple shear curves along RD–ND and TD–ND planes.

the anisotropic plastic response of textured metals for macroscale modeling. This criterion is applicable to materials that exhibit strength differential effects (e.g. Mg) as well as to materials for which there is no noticeable difference in behavior between tension and compression during monotonic loading (e.g. Al). The essential features of the model are summarized below. The anisotropic yield criterion is an extension to orthotropy of Cazacu et al. (2006) isotropic yield function, which is expressed as:

$$G(S_1,S_2,S_3,k,a) = (|S_1| - kS_1)^a + (|S_2| - kS_2)^a + (|S_3| - kS_3)^a, \quad (12)$$

where S_1, S_2 and S_3 are the principal values of the stress deviator $S = \sigma - \frac{1}{3}tr(\sigma)\,\mathbf{I}$ (tr being the trace operator and $\mathbf{I}$ the 2nd order identity tensor) while a and k are material parameters. Starting from the isotropic function (12), anisotropy is then introduced through two linear transformations operating on the Cauchy stress deviator S. The general form of the CPB06ex2 anisotropic criterion is:

$$F(\Sigma,\Sigma',k,a) = G(\Sigma_1,\Sigma_2,\Sigma_3,k,a) + G(\Sigma'_1,\Sigma'_2,\Sigma'_3,k',a). \quad (13)$$

In Eq. (13), k and k' are material parameters that allow for the description of strength differential effects, a is the degree of homogeneity, $(\Sigma_1,\Sigma_2,\Sigma_3)$ and $(\Sigma'_1,\Sigma'_2,\Sigma'_3)$ are the principal values of the transformed tensors

$$\Sigma = C : S \quad \text{and} \quad \Sigma' = C' : S, \quad (14)$$

respectively and ":" denotes the doubly contracted product of the two tensors. The restrictions imposed on the linear fourth-order operations C and C' are to satisfy the major and minor symmetries and to be invariant with respect to the orthotropy group (for rolled sheet simulations).

Let (x,y,z) be the reference frame associated with orthotropy. In the case of a sheet, x, y, and z represent the rolling, transverse, and the normal directions. Relative to the orthotropy axes (x,y,z), the fourth-order tensors C and C' operating on the stress deviator are represented in Voigt notations by:

$$C = \begin{bmatrix} C_{11} & C_{12} & C_{13} & 0 & 0 & 0 \\ C_{12} & C_{22} & C_{23} & 0 & 0 & 0 \\ C_{13} & C_{23} & C_{33} & 0 & 0 & 0 \\ 0 & 0 & 0 & C_{44} & 0 & 0 \\ 0 & 0 & 0 & 0 & C_{55} & 0 \\ 0 & 0 & 0 & 0 & 0 & C_{66} \end{bmatrix},$$

$$C' = \begin{bmatrix} C'_{11} & C'_{12} & C'_{13} & 0 & 0 & 0 \\ C'_{12} & C'_{22} & C'_{23} & 0 & 0 & 0 \\ C'_{13} & C'_{23} & C'_{33} & 0 & 0 & 0 \\ 0 & 0 & 0 & C'_{44} & 0 & 0 \\ 0 & 0 & 0 & 0 & C'_{55} & 0 \\ 0 & 0 & 0 & 0 & 0 & C'_{66} \end{bmatrix}.$$

Thus, for 3D stress and orthotropic symmetry, the tensors C and C' involved in the orthotropic criterion (13) each have nine non-zero components. When diagonal components of C and C' are set to unity and all the other components are zero, this orthotropic yield function reduces to the isotropic yield function (12). Note that when

$C = C'$ and $k = k'$, the criterion reduces to the anisotropic yield criterion of Cazacu et al. (2006). If the yield in tension is equal to the yield in compression, the parameters k and k' associated with strength differential effects are automatically zero. In addition, for $k = k' = 0$, $C = C'$ and $a = 2$, the anisotropic criterion (13) reduces to Hill (1948) orthotropic criterion. In other words, the above generalized criterion is applicable to asymmetric and anisotropic materials and includes, as special cases of isotropic, Hill (1948) anisotropic and Cazacu et al. (2006) anisotropic criteria.

5.1. Calibration of CPB06ex2 yield function for cubic materials

In Plunkett et al. (2008) the physical significance of the coefficients involved in the CPB06ex2 criterion and an identification procedure based on the results of tensile and compression tests has been outlined. In this paper, the equations and identification procedures for CPB06ex2 *tailored only for cubic materials* are presented. As already mentioned, cubic materials do not exhibit tension/compression asymmetry, thus the material parameters associated with strength differential effects are automatically zero, i.e. $k = 0$ and $k' = 0$ (see (13)) and the effective stress associated with the CPB06ex2 orthotropic yield condition can be written in the form:

$$\sigma_{\text{eff}} = \left(|\Sigma_1|^a + |\Sigma_2|^a + |\Sigma_3|^a + |\Sigma'_1|^a + |\Sigma'_2|^a + |\Sigma'_3|^a\right)^{1/a}. \tag{15}$$

Thus, the yield function CPB06-ex2 contains 18 parameters which are all related to the description of the anisotropy of the respective cubic material. However, since the yield function (15) is homogeneous of degree one in its arguments, without loss of generality we can set $C_{11} = C'_{11} = 1$. The remaining 10 coefficients C_{ij}, C'_{ij}, with $i,j = 1,\ldots,3$ and C_{66}, C'_{66}, are related to the in-plane properties of the sheet. These can typically be determined by conducting uniaxial tension tests at every 15° from the rolling direction, giving seven yield stresses and R-values. Alternatively, they can be determined from crystal plasticity calculations if the crystallographic texture of the material is measured.

Indeed, for 2D plane stress conditions (i.e. stress tensor $\sigma = (\sigma_{xx}, \sigma_{yy}, \sigma_{zz}, \sigma_{xy})$ comprised of four non-zero components), the tensors C and C' are represented relative to the orthotropy axes (x,y,z) by the 4×4 matrices

$$C = \begin{bmatrix} C_{11} & C_{12} & C_{13} & \\ C_{12} & C_{22} & C_{23} & \\ C_{13} & C_{23} & C_{33} & \\ & & & C_{66} \end{bmatrix} \quad \text{and} \quad C' = \begin{bmatrix} C'_{11} & C'_{12} & C'_{13} & \\ C'_{12} & C'_{22} & C'_{23} & \\ C'_{13} & C'_{23} & C'_{33} & \\ & & & C'_{66} \end{bmatrix}.$$

To simplify the equations we introduce the following notations:

$$\begin{aligned} \Phi_1 &= \frac{1}{3}(2C_{11} - C_{12} - C_{13}), \quad \Phi_2 = \frac{1}{3}(2C_{12} - C_{22} - C_{23}), \\ \Phi_3 &= \frac{1}{3}(2C_{13} - C_{23} - C_{33}), \\ \Psi_1 &= \frac{1}{3}(-C_{11} + 2C_{12} - C_{13}), \quad \Psi_2 = \frac{1}{3}(-C_12 + 2C_{22} - C_{23}), \\ \Psi_3 &= \frac{1}{3}(-C_{13} + 2C_{23} - C_{33}). \end{aligned} \tag{16}$$

Accordingly, the principal values of the transformed tensor Σ are given by

$$\begin{aligned} \Sigma_1 &= \frac{1}{2}\left(\Sigma_{xx} + \Sigma_{yy} + \sqrt{(\Sigma_{xx} - \Sigma_{yy})^2 + 4\Sigma^2_{xy}}\right), \\ \Sigma_2 &= \frac{1}{2}\left(\Sigma_{xx} + \Sigma_{yy} - \sqrt{(\Sigma_{xx} - \Sigma_{yy})^2 + 4\Sigma^2_{xy}}\right), \\ \Sigma_3 &= \Sigma_{zz}, \end{aligned} \tag{17}$$

where

$\Sigma_{xx} = \Phi_1\sigma_{xx} + \Psi_1\sigma_{yy}$, $\Sigma_{yy} = \Phi_2\sigma_{xx} + \Psi_2\sigma_{yy}$,
$\Sigma_{xy} = C_{66}\sigma_{xy}$, $\Sigma_{zz} = \Phi_3\sigma_{xx} + \Psi_3\sigma_{yy}$ (see also notations (16)).

Similarly, the principal values of the transformed tensor Σ' are expressed in terms of the components $\Sigma'_{xx}, \Sigma'_{xy}, \Sigma'_{yy}, \Sigma'_{zz}$ through relations similar to (17) using notations similar to (15) for defining $\Phi'_1, \Phi'_2, \Phi'_3$ in terms of the anisotropy coefficients C'_{ij}. Let σ_θ denote the yield stress in a direction at angle θ from the rolling direction x. According to the criterion (see Eq. (15)):

$$\sigma_\theta = \sigma_0\left\{\frac{|\Phi_1|^a + |\Phi_2|^a + |\Phi_3|^a + |\Phi'_1|^a + |\Phi'_2|^a + |\Phi'_3|^a}{|A_1|^a + |A_2|^a + |A_3|^a + |A'_1|^a + |A'_2|^a + |A'_3|^a}\right\}^{\frac{1}{a}}, \tag{18}$$

where σ_0 is the tensile yield stress in the rolling direction (i.e. for $\theta = 0$),

$$\begin{aligned} A_1 &= \frac{1}{2}\Big((\Phi_1 + \Phi_2)\cos^2\theta + (\Psi_1 + \Psi_2)\sin^2\theta \\ &\quad + \sqrt{\left((\Phi - \Phi_1)\cos^2\theta + (\Psi - \Psi_1)\sin^2\theta\right)^2 + 4C^2_{66}\sin^2\theta\cos^2\theta}\Big), \\ A_2 &= \frac{1}{2}\Big((\Phi_1 + \Phi_2)\cos^2\theta + (\Psi_1 + \Psi_2)\sin^2\theta \\ &\quad - \sqrt{\left((\Phi_1 - \Phi_2)\cos^2\theta + (\Psi_1 - \Psi_2)\sin^2\theta\right)^2 + 4C^2_{66}\sin^2\theta\cos^2\theta}\Big), \\ A_3 &= \Phi_3\cos^2\theta + \Psi_3\sin^2\theta, \end{aligned} \tag{19}$$

and Φ_1, Φ_2, Φ_3 and Ψ_1, Ψ_2, Ψ_3 are given by notations (16).

Relations similar to (19) express A'_1, A'_2, A'_3 in terms of the angle θ and the anisotropy coefficients C'_{ij}, respectively. In particular, the yield stress at 90° is expressed as:

$$\sigma_{90} = \sigma_0\left\{\frac{|\Phi_1|^a + |\Phi_2|^a + |\Phi_3|^a + |\Phi'_1|^a + |\Phi'_2|^a + |\Phi'_3|^a}{|\Psi_1|^a + |\Psi_2|^a + |\Psi_3|^a + |\Psi'_1|^a + |\Psi'_2|^a + |\Psi'_3|^a}\right\}^{\frac{1}{a}}. \tag{20}$$

For biaxial stress conditions, yielding occurs when $\sigma_{xy} = 0$ and $\sigma_{xx} = \sigma_{yy} = \sigma_b$, where

$$\sigma_b = \sigma_0\left\{\frac{|\Phi_1|^a + |\Phi_2|^a + |\Phi_3|^a + |\Phi'_1|^a + |\Phi'_2|^a + |\Phi'_3|^a}{|\Omega_1|^a + |\Omega_2|^a + |\Omega_3|^a + |\Omega'_1|^a + |\Omega'_2|^a + |\Omega'_3|^a}\right\}^{\frac{1}{a}}, \tag{21}$$

with $\Omega_1 = \left(\frac{1}{3}C_{11} + \frac{1}{3}C_{12} - \frac{2}{3}C_{13}\right)$, $\Omega_2 = \frac{1}{3}(C_{12} + C_{22} - 2C_{23})$, $\Omega_3 = \frac{1}{3}(C_{13} + C_{23} - 2C_{33})$ and similar expressions for the $\Omega'_1, \Omega'_2, \Omega'_3$.

Furthermore, we assume that the plastic potential coincides with the yield function. Let r_θ denote the strain value (width to thickness strain ratios) under uniaxial tensile loading in a direction at angle θ from the rolling direction in the (xy) plane.

$$r_\theta = -\frac{\sin^2\theta\frac{\partial\sigma_{\text{eff}}}{\partial\sigma_{xx}} - \sin(2\theta)\frac{\partial\sigma_{\text{eff}}}{\partial\sigma_{xy}} + \cos^2\theta\frac{\partial\sigma_{\text{eff}}}{\partial\sigma_{yy}}}{\frac{\partial\sigma_{\text{eff}}}{\partial\sigma_{xx}} + \frac{\partial\sigma_{\text{eff}}}{\partial\sigma_{yy}}}, \tag{22}$$

where σ_{eff} is given by (15). In particular, according to the criterion, the strain ratio in the rolling direction is

$$r_0 = -\frac{\Lambda_1 + \Lambda'_1}{\Lambda_2 + \Lambda'_2}, \tag{23}$$

where

$$\begin{aligned} \Lambda_1 &= \Phi_1^{a-1}\Psi_1 + (-1)^a\left(\Phi_2^{a-1}\Psi_2 + \Phi_3^{a-1}\Psi_3\right), \\ \Lambda_2 &= \Phi_1^{a-1}(\Psi_1 + \Phi_1) + (-1)^a\left(\Phi_2^{a-1}\Psi_2 + \Phi_3^{a-1}\Psi_3 + \Phi_2^a + \Phi_3^a\right), \end{aligned}$$

with similar expressions for Λ'_1 and Λ'_2. The strain ratio in the transverse direction is given by:

$$r_{90} = -\frac{\Lambda_3 + \Lambda'_3}{\Lambda_4 + \Lambda'_4}, \tag{24}$$

with

$$\Lambda_3 = -\Psi_2^{a-1}\Phi_2 + (-1)^a\left(\Psi_1^{a-1}\Phi_1 + \Psi_3^{a-1}\Phi_3\right),$$
$$\Lambda_4 = -\Psi_2^{a-1}(\Phi_2 + \Psi_2) + (-1)^a\left(\Psi_1^{a-1}\Phi_1 + \Psi_3^{a-1}\Phi_3 + \Psi_1^a + \Psi_3^a\right),$$

with similar expressions for Λ'_3 and Λ'_4. The in-plane shear coefficients may be determined using theoretical expression of the yield stress in pure shear in the sheet plane

$$\tau_{xy} = \frac{\sigma_0}{2}\left\{\frac{|\Phi_1|^a + |\Phi_2|^a + |\Phi_3|^a + |\Phi'_1|^a + |\Phi'_2|^a + |\Phi'_3|^a}{|C_{66}|^a + |C'_{66}|^a}\right\}^{\frac{1}{a}}. \quad (25)$$

In conclusion, using Eqs. (18)–(25), the coefficients C_{ij}, C'_{ij}, with $i,j = 1,\ldots,3$ and C_{44}, C'_{44} of the yield criterion (15) can be determined by minimizing an error function of the form

$$\text{Error} = \sum_n \text{weight}\left(1 - \frac{\sigma^n_{\text{th}}}{\sigma^n_{\text{data}}}\right)^2 + \sum_m \text{weight}\left(1 - \frac{r^m_{\text{th}}}{r^m_{\text{data}}}\right)^2. \quad (26)$$

In the above equation, the subscript "data" may refer to either points obtained from direct measurements (uniaxial loading tests) or virtual tests using crystal plasticity simulations.

The four remaining parameters $C_{44}, C_{55}, C'_{44}, C'_{55}$ which are associated with out-of-plane properties may be determined based on out-of-plane data such as yield stress for simple shear in the *yz* and *zx* planes and uniaxial tension at 45° between *y* and *z*, and between *z* and *x*.

According to the criterion, the yield stress in pure shear in the planes (*xz*) and (*yz*) are:

$$\tau_{yz} = \frac{\sigma_0}{2}\left\{\frac{|\Phi_1|^a + |\Phi_2|^a + |\Phi_3|^a + |\Phi'_1|^a + |\Phi'_2|^a + |\Phi'_3|^a}{|C_{44}|^a + |C'_{44}|^a}\right\}^{\frac{1}{a}}, \quad (27)$$
$$\tau_{xz} = \frac{\sigma_0}{2}\left\{\frac{|\Phi_1|^a + |\Phi_2|^a + |\Phi_3|^a + |\Phi'_1|^a + |\Phi'_2|^a + |\Phi'_3|^a|}{C_{55}|^a + |C'_{55}|^a}\right\}^{\frac{1}{a}}.$$

These properties cannot be easily measured for sheets. However these data points can be determined by the use of crystal plasticity calculations. If simulated data are not to be available, an alternative is to approximate the remaining parameters by setting them to their isotropic values.

It is to be noted that the anisotropy coefficients C_{ij}, C'_{ij} do not have any direct correlation with texture features.

6. Results and discussion

Two procedures for calibrating the anisotropy parameters were tested and evaluated. In the first approach, denoted as "Fit 1", the FE per grain crystal plasticity simulations are used to calculate yield data points and R-ratios along seven orientations 0°, 15°, 30°, 45°, 60°, 75° and 90°.

In the second approach, "Fit 2", measured directional yield stresses and *r*-ratios corresponding to the same seven orientations obtained from uniaxial tensile tests are used in the calibration. Tables 4 and 5 show the values of the anisotropy constants C_{ij}, C'_{ij}, with $i,j = 1,\ldots,3$ (the anisotropy coefficients associated with in-plane properties) for the CC AA5754 aluminum sheets using these calibration procedures.

Table 4
(Coefficients for Fit 1): $a = 2.796$.

C_{12}	C_{13}	C_{22}	C_{23}	C_{33}	C_{66}
−2.592	−5.48	1.087	−7.806	−6.16	4.762
C'_{12}	C'_{13}	C'_{22}	C'_{23}	C'_{33}	C'_{66}
−1.93	−4.541	6.687	−0.457	2.663	6.779

Table 5
(Coefficients for Fit 2): $a = 2.891$.

C_{12}	C_{13}	C_{22}	C_{23}	C_{33}	C_{66}
−1.928	−4.943	−0.474	−7.132	−5.586	4.904
C'_{12}	C'_{13}	C'_{22}	C'_{23}	C'_{33}	C'_{66}
−0.254	−2.277	6.715	7.606	4.437	5.226

The anisotropy of the normalized yield stress (ratio of the directional yield stress to the yield stress in the rolling direction) using the two fits are shown in Figs. 10 and 11 along with the data points obtained from direct measurements. The strength anisotropy of the alloy is moderate and varies within a 5% range. However, the variation of the directional yield stress with the tensile direction is quite complex in Fig. 10. The crystal plasticity model and the analytical model using crystal plasticity data (Fit 1) show the same trends as the experimental data, with minimum yield stress for the sample with tensile axis at 60° from the rolling direction. Since yield strength is determined mainly by initial texture, it is safe to conclude that the effect of initial texture on the stress ratio anisotropy is satisfactorily captured even if only crystal plasticity data are used for calibration. The yield function using Fit 2 captures the yield ratio more accurately than Fit 1 but the differences are

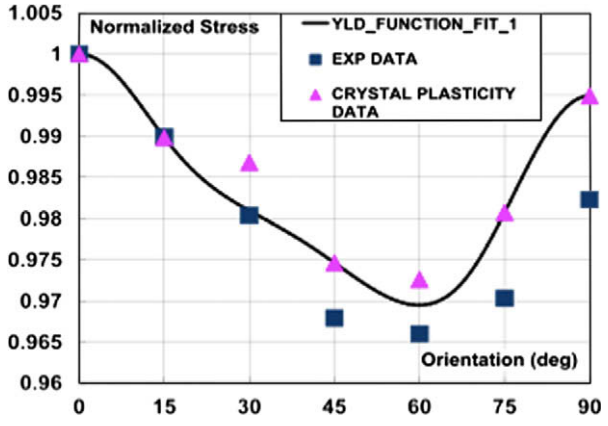

Fig. 10. Yield stress variation according to the yield criterion (12) calibrated using solely crystal plasticity data in comparison with the mechanical test results and crystal plasticity data.

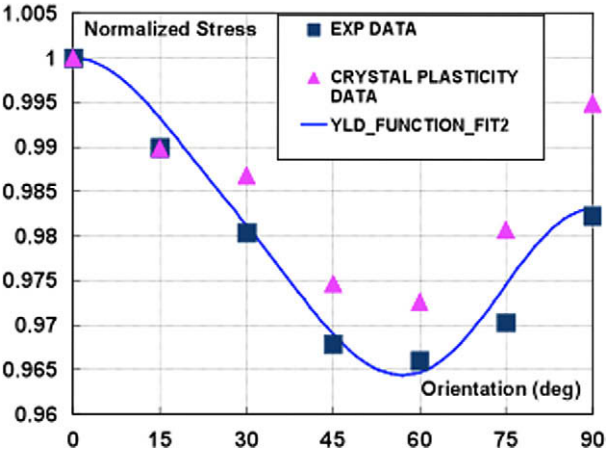

Fig. 11. Yield stress variation according to the yield criterion (12) calibrated using only mechanical test results in comparison with the experimental and crystal plasticity data.

such that crystal plasticity approach can be a substitute for the elaborate experimental measurement of yielding anisotropy.

The variation of the strain ratio r_θ with respect to the rolling direction is shown in Figs. 12 and 13. The experimental variation of the strain ratio is very strong; the lowest value of r_θ occurs for the sample with tensile axis 30° away from the rolling direction and highest in the transverse direction of the plate (at 90°). The variation in the value of r_θ between the lowest and the highest values is nearly 100%, fluctuating between 0.54 and 1.08. Both Fit 1 and Fit 2 of the phenomenological criterion, calibrated using only crystal plasticity data and mechanical test results, describe the anisotropy of the material well.

For certain alloys and textures, the predictions of the *R*-values anisotropy according to the classical Taylor-type polycrystal model (i.e. assumption of homogeneous deformation) may not be accurate (see for example the *R*-value distribution for AA 6022-T4 sheet reported in Cazacu and Barlat (2003)). For other alloys, *R*-value anisotropy is well reproduced both qualitatively and quantitatively (see Guan et al. (2008)). In this paper, we show that with a more advanced description of crystal plasticity, the *R*-value predictions are improved; the FE per grain crystal plasticity simulation reproduces the *R*-value anisotropy, showing r_{90} higher than r_{45} and r_0 (Inal et al. (2000)) in rolled sheets. It is safe to say that the texture evolution has been properly accounted for in the crystal plasticity model and that experiments can be bypassed when crystal plasticity results are used to calibrate the macromodel.

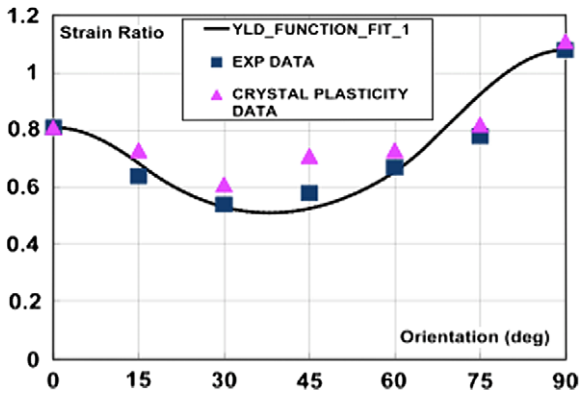

Fig. 12. Strain ratio variation according to the yield criterion (12) calibrated using solely crystal plasticity data (Fit 1) in comparison with the mechanical test results and crystal plasticity data.

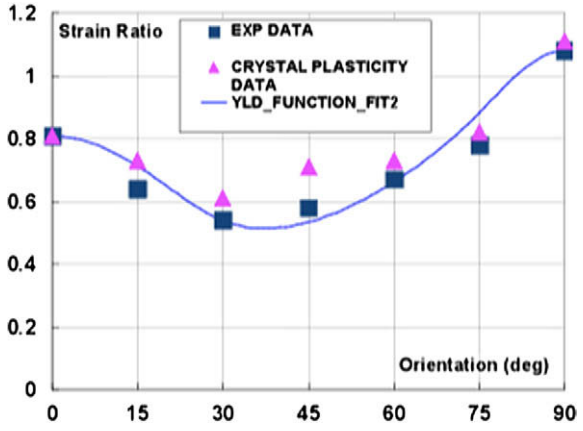

Fig. 13. Strain ratio variation according to the yield criterion (12) calibrated using solely experimental data (Fit 2) in comparison with the mechanical test results and crystal plasticity data.

These results demonstrate that the yield criterion (15) is flexible enough to describe accurately both the *R*-value and yield stress anisotropy simultaneously. Fig. 14 shows the representation in the biaxial plane ($\sigma_{xy} = 0$) of the yield surfaces according to CPB06ex2 corresponding to Fit 1 and Fit 2, respectively.

Fit 1 of the phenomenological criterion, which was calibrated using only crystal plasticity obtained yield stresses and strain ratios at 0, 15, 45, 75 and 90 describes very well the overall trend of the yield stress variation (see Fig. 10). Concerning the anisotropy of the strain ratio i.e. plastic flow anisotropy, Fit 2 of the criterion describes very well the experimental data. Fit 1, which is calibrated using solely crystal plasticity data, describes qualitatively the experimental trends (overestimate the experimental *R*-values by 5–10%). The yield function calibrated with crystal plasticity data and the yield function calibrated with the experimental data are interchangeable for stress ratio calculations and strain ratio calculations and one can use the results of crystal plasticity simulations instead of experimental data confidently. In other words, only crystal plasticity data that can capture correctly *R*-values may replace mechanical tests for identification/characterization purposes. Using only biaxial crystal plasticity data to calibrate the macroscopic yield function may lead to a less precise description of the plastic anisotropy at the macroscopic level (see also Grytten et al. (2008); Rousselier et al. (2009); etc.).

From the results presented above, it may be inferred that using directional yield stresses and strain ratios in seven different orientations obtained with FE per grain crystal plasticity model to calibrate the macroscopic yield criterion provides a very good approach to describe the overall behavior of the material in macroscale forming operations.

7. Summary and conclusions

In this paper, it was shown that accurate crystal plasticity model based only on initial texture data and a single stress–strain curve can describe with accuracy the anisotropic mechanical response of FCC alloy sheets. Thus, it becomes possible to replace mechanical characterization tests with virtual tests for identification of the anisotropy coefficients involved in macroscopic scale yield functions and furthermore use these yield function for design applications. The accuracy of the FE crystal plasticity predictions is due to the use of the "finite element per grain" unit cell model. In particular, it is shown that the polycrystal calculations capture the stress–strain hardening curves in all the orientations and the

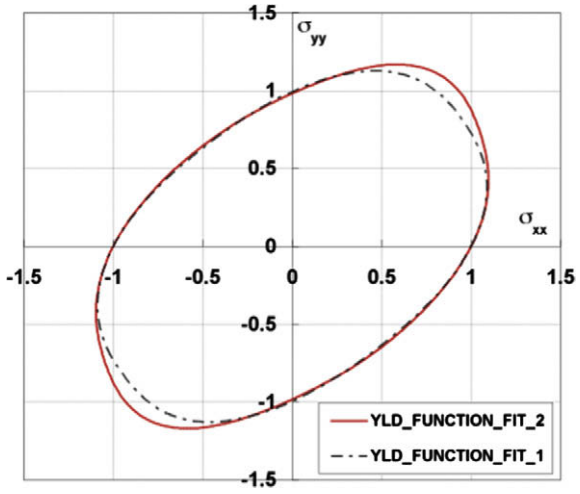

Fig. 14. Biaxial projection of the yield surfaces according to CPB06ex2 calibrated using only mechanical data (Fit 1) and using crystal plasticity data (Fit 2).

anisotropic distribution of the *R*-values (width to thickness strain ratios) can be in excellent agreement with the experimental *R*-values with the choice of the hardening law. Simulations demonstrate that for a single strain path (uniaxial tension in this case), the simple so-called power-law hardening law was able to reproduce the stress–strain curves correctly with only three material parameters to be determined. However *R*-value predictions required more complex hardening laws to be implemented to reproduce subtle differences between RD, 45° and TD samples. In this paper, Plunkett et al. (2008) yield function was used and applied to analyze the plastic anisotropy of a continuous cast AA5754 sheets, yet the proposed methodology is general and can be applied to any yield function and any FCC alloy sheet. The results presented above represent the first robust demonstration of implementing microscale crystal plasticity simulation with measured texture data and hardening laws in macroscale yield criterion simulations in an accurate manner and should be of broader interest to the metal forming community.

Finally, it should be mentioned that our future plans include using the approach presented in the paper for Mg alloys. In contrast with aluminum alloys discussed in this paper, there is a strong texture evolution in Mg alloys which is stress-path dependent. It is believed that only by explicitly modeling the different mechanisms (already introduced in the present model), this evolution may be captured.

Acknowledgements

This work was supported by the Natural Sciences and Engineering Research Council of Canada (NSERC), General Motors Research and Development Center in Warren, MI, and General Motors of Canada.

References

Asaro, R.J., Needleman, A., 1985. Texture development and strain hardening in rate dependent polycrystals. Acta Metall. 33, 923–953.
Barlat, F., Maeda, Y., Chung, K., Yanagawa, M., Brem, J.C., Hayashida, Y., Lege, D.J., Matsui, K., Murtha, S.J., Hattori, S., Becker, R.C., Makosey, S., 1997. Yield function development for aluminum alloy sheets. J. Mech. Phys. Solids 45, 1727–1763.
Barlat, F., Brem, J.C., Yoon, J.W., Chung, K., Dick, R.E., Lege, D.J., Pourboghrat, F., Choi, S.-H., Chu, E., 2003. Plane stress yield function for aluminum alloy sheet – Part I: theory. Int. J. Plast. 19, 1297–1319.
Barlat, F., Aretz, H., Yoon, J.W., Karabin, M.E., Brem, J.C., Dick, R.E., 2005. Linear transformation-based anisotropic yield functions. Int. J. Plast. 21, 1009–1039.
Barlat, F., Yoon, J.W., Cazacu, O., 2007. On linear transformations of stress tensors for the description of plastic anisotropy. Int. J. Plast. 23, 876–896.
Bassani, J.L., Wu, T., 1991. Latent hardening in single crystals – II: analytical characterisation and predictions. Proc. Roy. Soc. Lond. A435, 21–41.
Cazacu, O., Barlat, F., 2001. Generalization of Drucker's yield criterion to orthotropy. Math. Mech. Solids 6, 613–630.
Cazacu, O., Barlat, F., 2003. Application of the theory of representation to describe yielding of anisotropic aluminum alloys. Int. J. Eng. Sci. 41, 1367–1385.
Cazacu, O., Barlat, F., 2004. A criterion for description of anisotropy and yield differential effects in pressure-insensitive metals. Int. J. Plast. 20, 2027–2045.
Cazacu, O., Plunkett, B., Barlat, F., 2006. Orthotropic yield criterion for hexagonal close packed metals. Int. J. Plast. 22, 1171–1194.
Chang, Y.W., Asaro, R.J., 1981. An experimental study of shear localisation in Aluminium–Copper single crystals. Acta Metall. 29, 241–257.
Darrieulat, M., Montheillet, F., 2003. A texture based continuum approach for predicting the plastic behaviour of rolled sheet. Int. J. Plast. 19, 517–546.
Grytten, F., Holmedal, B., Hopperstad, O.S., Brvik, T., 2008. Evaluation of identification methods for YLD2004-18p. Int. J. Plast. 24, 2248–2277.
Guan, Y., Pourboghrat, F., Barlat, F., 2008. Finite element analysis of aluminum tube hydroforming based on non-quadratic yield function. Int. J. Manuf. Tech. Manag. 14, 84–99.
Hill, R., 1948. A theory of yielding and plastic flow of anisotropic metals. Proc. Roy. Soc. Lond. A193, 281–297.
Inal, K., Wu, P.D., Neale, K.W., MacEwen, S.R., 2000. Numerical simulation of large deformation polycrystalline plasticity. In: Martin, P., MacEwen, S., Verreman, Y., Liu, W.J., Goldak, J. (Eds.), Mathematical Modeling in Metal Processing and Manufacturing, MetSoc-CIM, p. 15.
Inal, K., Wu, P.D., Neale, K.W., 2002. Finite element analysis of localization in FCC polycrystalline sheets under plane stress tension. Int. J. Solids Struct. 39, 3469–3486.
Inal, K., Simha, M.H., Mishra, K.R., 2008. Numerical modeling of second-phase particle effects on localized deformation. J. Eng. Math. Tech. 130, 021003–021011.
Lebensohn, R.A., Tomé, C.N., 1993. A self-consistent anisotropic approach for the simulation of plastic deformation and texture development of polycrystals: application to zirconium alloys. Acta Metall. Mater. 41, 2611–2624.
Lopes, A.B., Barlat, F., Gracio, J.J., Ferreira Duarte, J.F., Rauch, E.F., 2003. Effect of texture and microstructure on strain hardening anisotropy for aluminum deformed in uniaxial tension and simple shear. Int. J. Plast. 19, 1–22.
Molinari, A., Canova, G.R., Ahzi, S., 1987. A self-consistent approach of the large deformation polycrystal viscoplasticity. Acta Metall. 35, 2983–2994.
Neale, K.W., Inal, K., Wu, P.D., 2003. Effects of texture gradients and strain paths on localization phenomena in polycrystals. Int. J. Mech. Sci. 45, 1671–1686.
Plunkett, B., Lebensohn, R.A., Cazacu, O., Barlat, F., 2006. Anisotropic yield function of hexagonal materials taking into account texture development and anisotropic hardening. Acta Mater. 54, 4159–4169.
Plunkett, B., Cazacu, O., Lebensohn, R.A., Barlat, F., 2007. Elastic–viscoplastic anisotropic modeling of textured metals and validation using the Taylor cylinder impact test. Int. J. Plast. 23, 1001–1021.
Plunkett, B., Cazacu, O., Barlat, F., 2008. Orthotropic yield criteria for description of the anisotropy in tension and compression of sheet metals. Int. J. Plast. 24, 847–866.
Rousselier, G., Barlat, F., Yoon, J.W., 2009. A novel approach for anisotropic hardening modeling. Part I: theory and its application to finite element analysis of deep drawing. Int. J. Plast. 25, 2383–2409.
Soare, S., Yoon, J.W., Cazacu, O., Barlat, F., 2007. Applications of a recently proposed anisotropic yield function to sheet forming. In: Banabic, D. (Ed.), Advanced Methods in Material Forming. Springer, pp. 131–149.
Soare, S., Yoon, J.W., Cazacu, O., 2008. On the use of homogeneous polynomials to develop anisotropic yield functions with applications to sheet forming. Int. J. Plast. 24, 915–944.
Tugcu, P., Neale, K.W., Wu, P.D., Inal, K., 2004. Crystal plasticity simulation of the hydrostatic bulge test. Int. J. Plast. 20, 1603–1653.
Wu, P.D., Inal, K., Neale, K.W., Kenny, L.D., Jain, M., MacEwen, S.R., 2001. Large strain behaviour of very thin aluminium sheets under planar simple shear. J. de Physique IV (11), 229–236.
Yoon, J.W., Barlat, F., Dick, R.E., 2004. Plane stress yield function for aluminum alloy sheet – Part II: FE formulation and its implementation. Int. J. Plast. 20, 495–522.
Yoon, J.W., Barlat, F., Dick, R.E., Karabin, M.E., 2006. Prediction of six or eight ears in a drawn cup based on a new anisotropic yield function. Int. J. Plast. 22, 174–193.
Yoshida, K., Kuwabara, T., Kuroda, M., 2007. Path-dependence of the forming limit stresses in a sheet metal. Int. J. Plast. 23, 361–384.